ADVANCED PHOTONICS RESEARCH
Open Access
www.adpr-journal.com

BODIPY-Pt-Porphyrins Polyads for Efficient Near-Infrared Light-Emitting Electrochemical Cells

Elisa Fresta, Asterios Charisiadis, Luca M. Cavinato, Nadia Palandjian, Kostas Karikis, Vasilis Nikolaou, Georgios Charalambidis, Athanassios G. Coutsolelos, and Rubén D. Costa**

The synthesis, characterization, and application in light-emitting electrochemical cells (LECs) of two near-infrared (NIR)-emitting Pt-porphyrins (Pt-por) with none or 20 F atoms and their respective Pt-por polyads containing from 1 to 4 BODIPY (BDP) units (PtBDP) connected via tetra-fluorophenyl triazole spacer groups are reported. The functionalization of PtBDPs is tuned with respect to the number of BDP units and F atoms optimizing 1) the NIR emission through an efficient energy transfer from the BDP to the Pt-por core, 2) the electronic structure to decouple charge transport via BDP and exciton formation at the Pt-por, and 3) the ionic conductivity in thin films. A comprehensive rationale on how the molecular design rules the device performance is provided, achieving LECs with emission at 780 nm. This is realized using PtBDP-2-8, in which a host:guest strategy between BDP and Pt-por in thin films is fully operative accompanied by an optimal ionic conductivity. This is supported by spectroelectrochemical findings and device analysis with both Pt-por references and the PtBDP series. Overall, this work highlights that Pt-porphyrins are efficient emitters in developing NIR LECs due to their rich functionalization, enabling to control charge transport, energy transfer, and ionic conductivities.

1. Introduction

The search for deep-red and near-infrared (NIR) small molecule emitters for solid-state lighting devices is an ongoing quest.[1,2] Among the solid-state lighting approaches, light-emitting electrochemical cells (LECs) are of particular interest as they consist of a simple structure, that is, a layer of ionic and neutral electroluminescent materials with ionic additives, sandwiched between two electrodes.[3,4] The working mechanism involves the initial formation of electric double layers (EDLs) upon applying external bias, leading to an efficient charge injection from air stable electrodes and the subsequent formation of p- and n-doped regions flanking the emitting undoped (i) region, in which hole–electron recombination forms radiative excitons. This working mechanism is named p–i–n junction. Importantly, the device performance does not strictly depend on the electrode material,[5] allowing for low-cost and high-throughput solution-based fabrication under ambient air.[3,6–8]

While several red emitters have already been implemented in LECs,[1,3,9–20] the best NIR-emitting LECs rely on ionic transition metal complexes.[9,21–27] Here, porphyrins could stand out due to their easy synthesis and modification toward NIR emission.[28] Indeed, several groups have recently shown interesting advances in porphyrin-based LECs. In 2016, our group first reported on the effect of the metal core (Zn^{2+}, Sn^{2+}, Pt^{2+}, and Pd^{2+}), of porphyrins on the LEC figures-of-merit, achieving red-emitting devices that were either stable and low efficient (Zn-porphyrin) or highly efficient but poorly stable (Pt-porphyrin).[17] In detail, Pt-porphyrin-based LECs exhibited good efficiencies caused by the heavy metal-induced phosphorescent emission, but also a pronounced electrochemical degradation, leading to low stabilities of a few minutes. This issue can be overcome using a host–guest system to decouple charge transport and exciton recombination.[11,17] In this context, the chemical binding of host–guest units in a dyad-type structure is desired over simple physical blending toward stable and efficient LECs.[11,15,29] For instance, we reported on intramolecular host–guest systems binding 1 BODIPY (BDP) unit to the periphery of a Zn-porphyrin that yielded deep-red LECs with one order of magnitude enhanced stabilities (>1000 h) keeping the low irradiance of the reference devices with the Zn-porphyrin reference.[11] Edman and coworkers reported on the design and synthesis of a host–guest star-shaped diketopyrrolopyrrole−Zn-porphyrin,

Dr. E. Fresta, L. M. Cavinato, Prof. R. D. Costa
Chair of Biogenic Functional Materials
Technical University of Munich
Schulgasse 22, 94315 Straubing, Germany
E-mail: ruben.costa@tum.de

Dr. A. Charisiadis, N. Palandjian, Dr. K. Karikis, Dr. V. Nikolaou, Dr. G. Charalambidis, Prof. A. G. Coutsolelos
Department of Chemistry
Laboratory of Bioinorganic Chemistry
University of Crete
Voutes Campus, Crete, Heraklion 70013, Greece
E-mail: acoutsol@uoc.gr

The ORCID identification number(s) for the author(s) of this article can be found under https://doi.org/10.1002/adpr.202000188.

DOI: 10.1002/adpr.202000188

realizing NIR emission (≈900 nm) along with good irradiances of 36 μW cm^{-2} and stabilities of tens of minutes.[15]

In view of these earlier reports, the molecular design of low-energy emitters following a host–guest strategy is very appealing toward realizing highly performing NIR LECs. Herein, we present the design of a series of Pt-porphyrin-**BDP** polyads by connecting 1, 2, 3, and 4 **BDP** units to the central porphyrin macrocycle through tetra-fluorophenyl triazole spacers (i.e., **PtBDP-*x*–*y*** in which *x* is the number of **BDP** and *y* is the number of F atoms) along with two reference Pt-porphyrins that bear either zero (**Pt-0**) or 20 F atoms at their peripheral substituents (**Pt-20**) (**Figure 1**). The rationale of this design is twofold. On one hand, the functionalization with fluorine and/or hexyloxy groups is an effective strategy to control the electronic properties that are further correlated to the LEC performance. Thus, we can elucidate clear relationships about the effect of coupling/decoupling charge transport process between the **BDP** and Pt-porphyrin units and the ionic conductivity in thin film via dipole–dipole interactions[11] on the device behavior. On the other hand, the covalent binding of increasing **BDP** units to the Pt-porphyrin core allows us to maximize the energy transfer from the **BDP** to the Pt-por in thin films.[30–32] This is supported by comprehensive spectroscopic, electrochemical, and microscopic studies that enable the correlation between molecular structure and electroluminescence features in LECs, namely, 1) the number of **BDP** units and the efficient energy transfer to the Pt-porphyrin to increase device efficiency, 2) the number of F atoms and the ionic conductivity in thin films allowing a well-balanced charge injection and transport to realize high irradiances and stable operation at low currents, and 3) the changes in the electronic structure toward an efficient host:guest design to decouple charge transport and recombination processes toward stable devices.

Among the members of this family, the best performing emitter was the **PtBDP-2-8**, exhibiting remarkable irradiances of ≈80 μW cm^{-2}, efficiencies of 0.12 lm W^{-1}, and stabilities of ≈1 h or 11 mJ, along with a NIR electroluminescence output centered at 780 nm. Overall, this work provides important guidelines for the design of highly performing porphyrin-based NIR LECs, highlighting how their rich chemical functionalization allows us to control charge transport, energy transfer, and ionic conductivities.

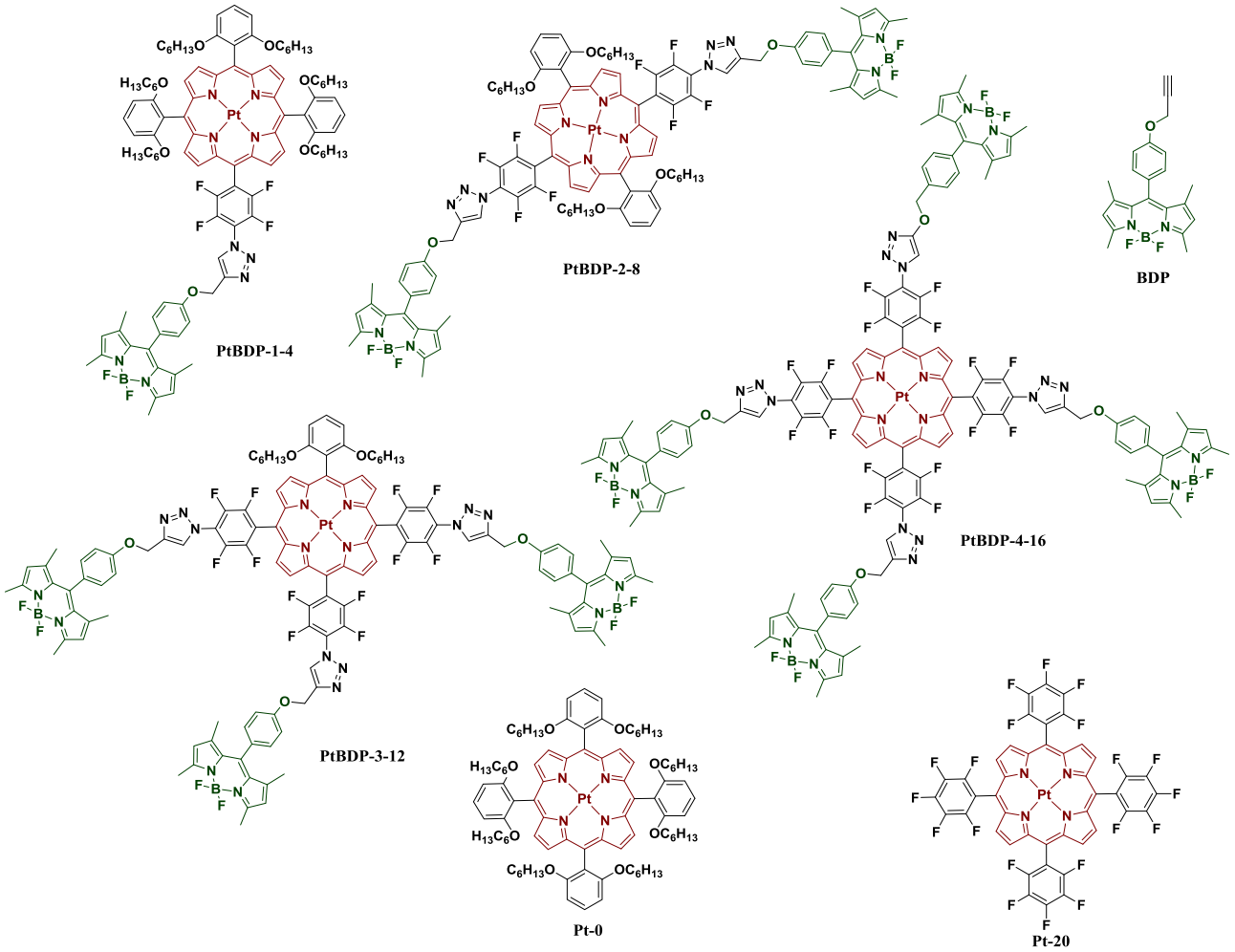

Figure 1. Chemical structures of reference compounds **BDP**, **Pt-0** and **Pt-20** as well as the new **PtBDP-*x*–*y*** polyads.

2. Results and Discussion

2.1. Synthesis

The synthesis of the PtBDP-1-4 is shown in **Scheme 1**. Porphyrin **1**[33] was metallated with Pt, providing derivative **2**, which was subsequently reacted with sodium azide in order for the *para*-fluorine atom to be replaced by the desired azide group, forming azide-porphyrin **3**. The final step was a click reaction between the azide bearing intermediate **3** and the alkyne-substituted BDP compound,[11] using CuI complex as the catalyst in a THF/CH_3CN (1:1) mixture, yielding **PtBDP-1-4**. This particular **BDP** compound was selected based on our previous study of Zn-porphyrin-BDP dyads, where the LECs with this nonconjugated (triazolyl)methoxy group between the **BDP** and the porphyrin outperformed the dyad, in which the two components were directly linked through the triazole ring.[11]

The experimental approach regarding **PtBDP-2-8** is shown in **Scheme 2**. At first, the *trans*-A_2B_2 porphyrin derivative 6 was prepared via a condensation reaction between dipyrromethane **4**[34] and aldehyde **5**[35] under mild conditions and the use of two oxidative reagents (BF_3OEt_2 and DDQ). The following two steps involved the insertion of the platinum metal center in the macrocycle core (**7**) and a nucleophilic aromatic substitution (SNAr) reaction for the substitution of *para*-fluorine atoms with —N_3 groups (**8**).[36] Finally, a copper-catalyzed (CuI) azide–alkyne cycloaddition was performed in a THF/CH_3CN (1:1) mixture, producing the **PtBDP-2-8**.

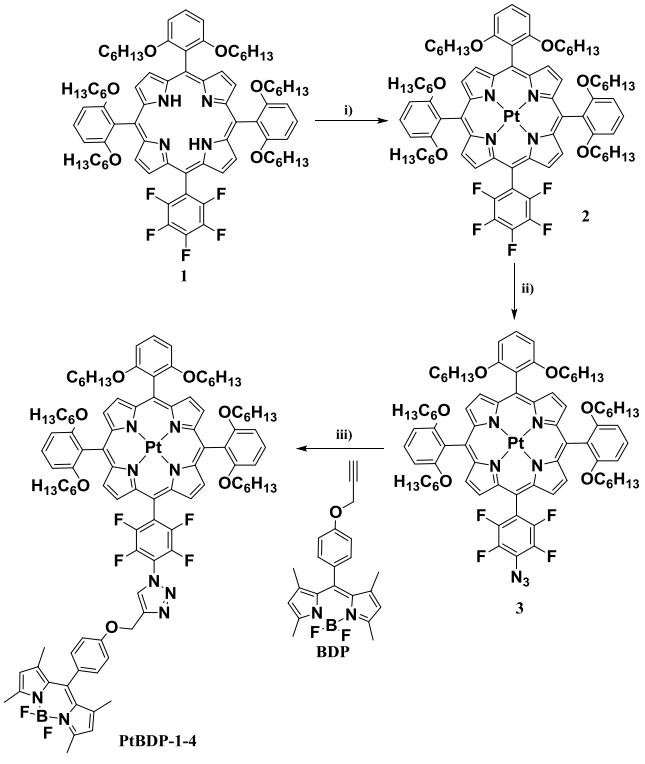

Scheme 1. Synthetic approach for the preparation of PtBDP-1-4. Conditions: i) $PtCl_2$, PhCN, reflux, 3 h; ii) NaN_3, DMF, 60 °C, 2 h; iii) DIPEA, CuI, THF/CH_3CN, N_2, RT, overnight.

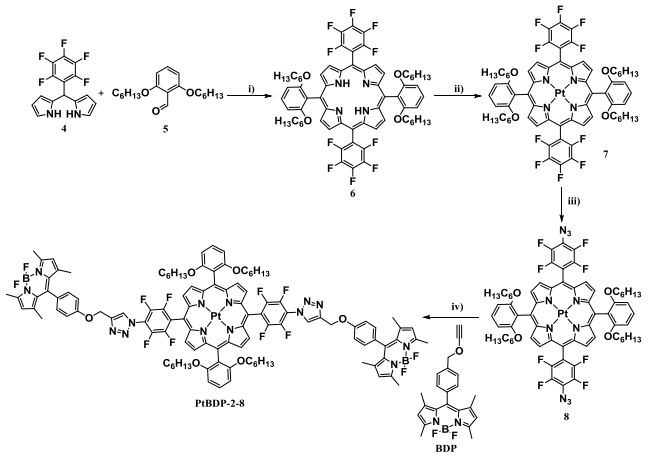

Scheme 2. Synthetic approach for the preparation of **PtBDP-2-8**. Conditions: i) $CHCl_3$, BF_3OEt_2, 24 h RT, DDQ, 20 h RT; ii) $PtCl_2$, PhCN, reflux, 3 h; iii) NaN_3, DMF, 60 °C, 2 h; iv) DIPEA, CuI, THF/CH_3CN, N_2, RT, overnight.

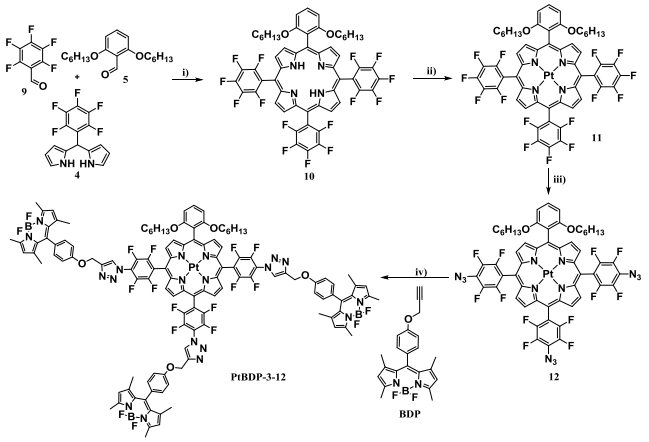

Scheme 3. Synthetic approach for the **PtBDP-3-12**. Conditions: i) $CHCl_3$, BF_3OEt_2, 24 h RT, DDQ, 20 h RT; ii) $PtCl_2$, PhCN, reflux, 3 h; iii) NaN_3, DMF, 60 °C, 2 h; iv) $CuSO_4{\cdot}5H_2O$, Sodium ascorbate, DMF/H_2O, 40 °C, 3 d.

The first step for the preparation of PtBDP-3-12 was the synthesis of tri-pentafluorophenyl-porphyrin **10** (**Scheme 3**). For this reaction, aldehydes **5** and **9** along with dipyrromethane **4** were stirred vigorously in a $CHCl_3$ solution for 44 h with the consecutive addition of BF_3OEt_2 (24 h) and DDQ (20 h). Then, we performed a metalation (porphyrin **11**) and a SNAr reaction (azide-containing intermediate 12). The last step was a CuAAC reaction, but with modified experimental conditions.[37] More specifically, the tri-azide-substituted Pt-por **12** was connected with the alkyne-BDP compound in the presence of sodium ascorbate and $CuSO_4{\cdot}5H_2O$ in a mixture of *N,N*-dimethylformamide (DMF) and water under heating at 40 °C. The reaction was completed after 3 days providing the desired product (PtBDP-3-12) with an 11% isolated yield.

Finally, the synthesis of the **PtBDP-4-16** hybrid is shown in **Scheme 4**. The reference porphyrin derivative **Pt-20** reacted with NaN_3 to form the symmetric tetra-N_3-porphyrinic compound **13**.

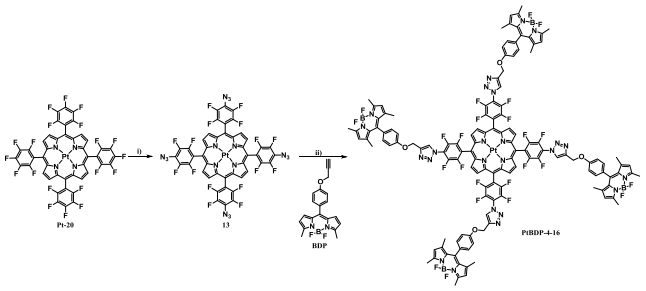

Scheme 4. Synthetic approach for **PtBDP-4-16**. Conditions: i) NaN_3, DMF, 60 °C, 2 h; ii) $CuSO_4{\cdot}5H_2O$, Sodium ascorbate, DMF/H_2O, 40 °C, 5 d.

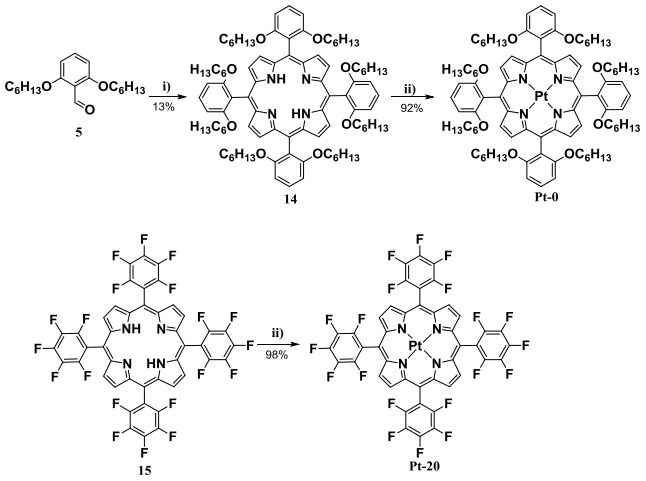

Scheme 5. Synthetic scheme for the preparation of **Pt-0** and **Pt-20**. Conditions: i) pyrrole, propionic acid, 3 h, reflux; ii) $PtCl_2$, PhCN, reflux, 3 h.

Lastly, for the preparation of **PtBDP-4-16** hybrid a click reaction between porphyrin **13** and BDP was performed, using the same experimental conditions as previously stated in the case of **PtBDP-3-12**.

The synthetic routes followed for the preparation of the reference porphyrins are shown in **Scheme 5**. In short, aldehyde **5** along with pyrrole underwent a typical Alder–Longo condensation reaction producing the symmetrical porphyrinic compound **14**. The following step is mutual for the synthesis of both reference complexes. Particularly, the free base porphyrins **14** and **15**[38] were metallated with platinum(II) chloride in benzonitrile under reflux, yielding the desired products Pt-0 and **Pt-20**, respectively.

The successful formation of all the intermediate and final products was verified through matrix-assisted laser desorption/ionization time-of-flight (MALDI-TOF) mass spectrometry and nuclear magnetic resonance (NMR) spectroscopy (^{1}H, ^{19}F, and ^{13}C) (Figure S1–S51, Supporting Information). Concerning the reference derivatives, their NMR spectra show typical peaks that correspond to symmetrical Pt-metallated porphyrins. In the ^{1}H NMR spectra of the final polyads, the characteristic proton signal of the formed triazole ring appeared at 8.33, 8.34, 8.36, and 8.38 ppm for **PtBDP-1-4** (Figure S13, Supporting Information), **PtBDP-2-8** (Figure S28, Supporting Information), **PtBDP-3-12** (Figure S42, Supporting Information), and **PtBDP-4-16** (Figure S48, Supporting Information), respectively. Finally, a characteristic quadruple BDP-based signal at approximately –146.3 ppm was detected in the ^{19}F NMR spectra of the final hybrids,[39] along with two additional signals (around –134.2 and –147.9 ppm), originating from the *ortho*- and *meta*-fluorine atoms of the porphyrin's peripheral phenyl groups.

2.2. Spectroscopic Studies in Solution and Thin Films

The UV–vis absorption features of the reference and polyads in both solution (THF) and thin films used for devices, namely, blends of each emitter with trimethylol propane ethoxylate (TMPE), and lithium triflate (LiOTf) in a mass ratio of emitter: TMPE:LiOTf 1:0.15:0.03, were studied (**Figure 2**) and **Table 1**. The ionic matrix was selected owing to the encouraging results obtained in the prior art.[13,14,40] The **BDP** shows the typical sharp and structured absorption band centered at 500 nm and an almost featureless spectrum in the high-energy region. However, the absorption spectra in thin films consist of two broad bands centered at 350 and 500 nm. This suggests that the films are highly aggregated, and they are, indeed, formed of crystalline domains as confirmed by optical microscopy images (Figure S52, Supporting Information). In stark contrast, the reference Pt-porphyrins exhibit a similar absorption band

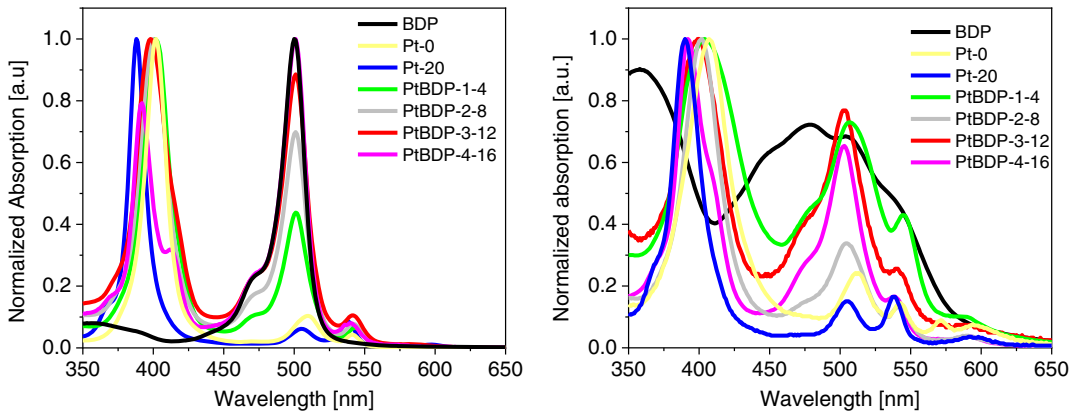

Figure 2. Absorption spectra of the reference and the polyad compounds (see legend) in THF 10^{-5} M (left) and thin-film onto quartz (right).

Table 1. Photophysical features of the reference compounds and the **PtBDP** polyads.

Compound	λ_{abs} [a] [nm]	λ_{abs} [b] [nm]	λ_{em} [b,c] [nm]	$<\tau>$ [b] [ns]	$<\tau>$ [b] [μs]	PLQY [b,d] [%]	$k_r \times 10^{-9}$ [s^{-1}]	$k_{nr} \times 10^{-9}$ [s^{-1}]
BDP	495	–	510[a]	3.5[a]	–	–	–	–
Pt-0	388	390	650, 729, 789	–	8.2	4.8[e]	5.8	115.3
PtBDP-1-4	401	404	511, 557, 653, 729	3.1	9.7	3.8	3.9	104.4
PtBDP-2-8	400	402	515, 552, 653, 729	1.3	9.9	3.5	3.5	96.5
PtBDP-3-12	399	399	515, 555, 654, 718	0.9	11.8	4.5	3.8	80.6
PtBDP-4-16	400	392	515, 552, 654, 718, 775	–	13.1	4.3	3.3	73.4
Pt-20	402	407	650, 708, 788	–	32.6	9.4[e]	2.9	27.9

[a]THF solution; [b]Thin film; [c]$\lambda_{exc} = 490$ nm; [d]$\lambda_{exc} = 490$ nm, $\lambda_{exc} = 400$ nm.

shape in thin film and solution. They consist of a Soret band centered around 400 nm and well-structured Q-bands peaking at ≈500, 540, and 580 nm (Figure 2). Importantly, there is no absorption features in the range of 450–480 nm, in which the **BDP** can exclusively be excited. In addition, the presence of the fluorine atoms in **Pt-20** leads to red-shifted absorption features,[41] while the absorption spectra of the thin films are slightly red-shifted compared with those in solution. Indeed, atomic force microscopy (AFM) images confirm that both films show a homogeneous morphology containing some aggregation features (Figure S53, Supporting Information). On the other hand, the **PtBDP** dyads feature a homogeneous film morphology without any aggregation that results in very similar absorption features in both solution and thin films (**Figure 3**). In short, characteristic peaks of both the Pt-porphyrin (≈400 nm and two less intense bands at ≈550 and 580 nm) and the **BDP** (≈500 nm) moieties are clearly detected. Thus, the absorption spectra can be described as a superimposition of the UV–vis spectra of the polyad constituents. As expected, the only difference in the absorption spectra of the final polyads concerns the intensity

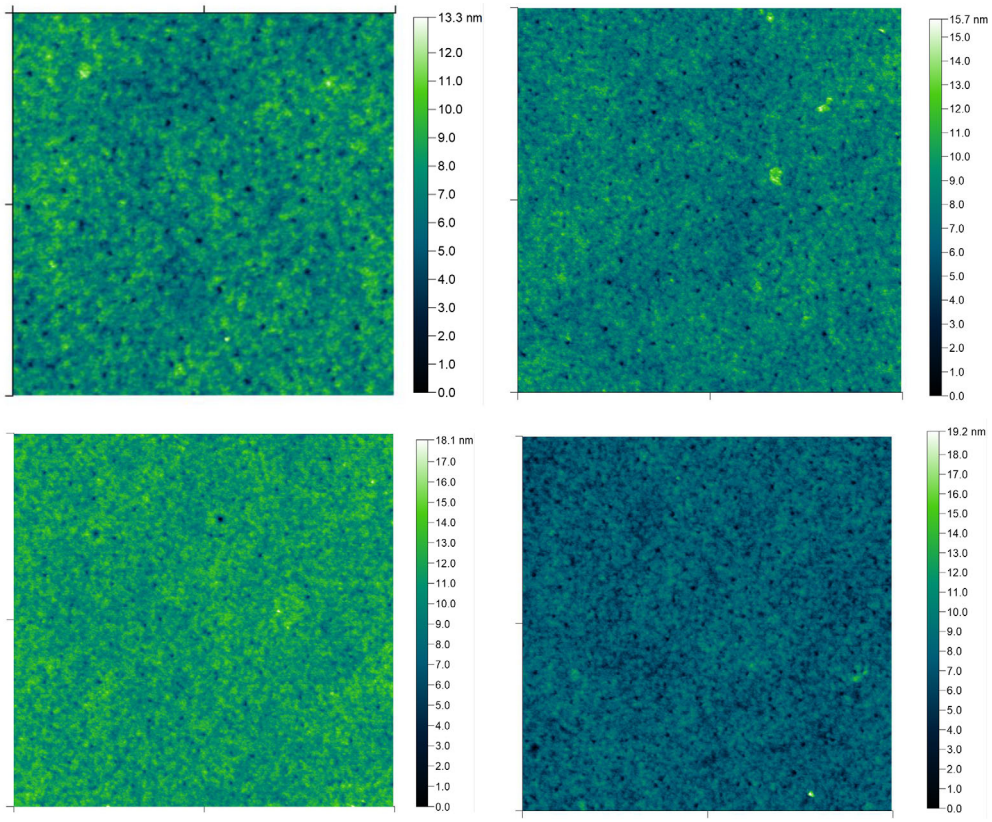

Figure 3. AFM images (10 × 10 μm) of the active layers of **PtBDP-1-4** (top left), **PtBDP-2-8** (top right), **PtBDP-3-12** (bottom left), and **PtBDP-4-16** (bottom right) as used in devices.

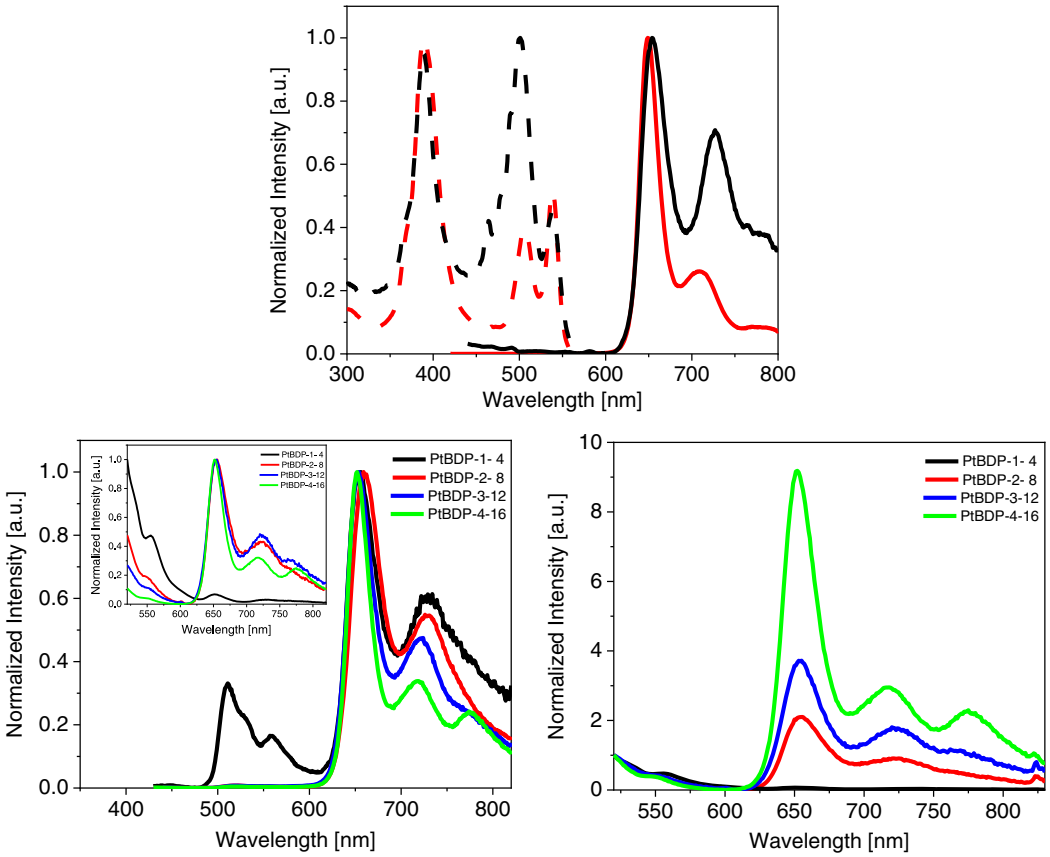

Figure 4. Top: Normalized emission (solid lines, λ_{exc} 490 nm) and excitation (dashed lines, λ_{em} 515 nm) spectra of **Pt-0** (black) and **Pt-20** (red) in thin films. Bottom: Normalized emission spectra of **PtBDP-*x*–*y*** (see legend) at $\lambda_{exc} = 400$ nm (left) and $\lambda_{exc} = 490$ nm (inset, left), as well as normalized emission spectra of **PtBDP-*x*–*y*** thin films ($\lambda_{exc} = 490$ nm) assuming the counts at 515 nm as 1 (right).

of the BDP-centered peak that tends to increase in relation to the increasing number of the peripheral BDP units that are connected to the porphyrin core (**Figure 4**).

As far as the photoluminescence in thin film is concerned, **BDP** and Pt-porphyrin references show the typical well-structured emission bands peaking at 500–600 and 600–800 nm, respectively (Figure 4 and S54, Supporting Information). The excitation spectra of **Pt-0** and **Pt-20** films show an intense peak around 510 nm, highlighting the possibility of an efficient energy transfer from the **BDP** to the porphyrin core in the polyads. Indeed, excitation at the **BDP** moiety ($\lambda_{exc} = 450$ nm) in **PtPBD** films leads to a dual emission centered at 515 nm (BDP) and at 650, 720, and 775 nm (Pt-porphyrin core) (Figure 4). Noteworthy, the high-energy emission band intensity decreases with respect to the overall emission spectrum upon increasing number of **BDP** units (e.g., 1 for **PtBDP-1-4** and 0.11 for **PtBDP-4-16**) (Figure 4). In addition, normalizing the data to the counts at $\lambda_{em} = 515$ nm shows a gradual increase in the emission intensity up to tenfold for **PtBDP-4-16** compared with **PtBDP-1-4** (Figure 4). Noteworthy, all these experiments were performed in thin films, in which the molecular conformations are frozen, and the energy transfer may lose efficiency compared with those in solution. However, it is in our interest to characterize the emitters in forms that resemble our devices.

To further corroborate the energy transfer process in thin films, the average excited-state lifetimes $<\tau>$ upon excitation at 395 nm and probing at 515 nm were measured. The BDP reference films showed a $<\tau>$ of 3.5 ns, while **PtBDP** arrays with 1, 2, and 3 BDP units showed a gradual decrease from 3.1, 1.3, and 0.9 ns, respectively. **PtBDP-4-16** did not show any detectable emission features at 515 nm and, in turn, any $<\tau>$ value (Table 1 and Figure S55, Supporting Information). The $<\tau>$ values related to the phosphorescence processes were investigated exciting with a microsecond lamp ($\lambda_{exc} = 400$ nm) and probing at 650 nm. The **Pt-0** and **Pt-20** films showed $<\tau>$ values of 8.2 and 32.6 µs, respectively. The longer $<\tau>$ in **Pt-20** is ascribed to a correspondent increase in the number of fluorine atoms in its periphery, which may stabilize the excited state via negative hyperconjugation.[41] Indeed, the **PtBDP** films showed an increasing trend in $<\tau>$ upon increasing the number of F atoms (Table 1 and Figure S56, Supporting Information).

Finally, the **Pt-0** and **Pt-20** films showed photoluminescence quantum yield (PLQY) ($\lambda_{exc} = 490$ nm) values of ≈5% and 10%, respectively. In contrast, the PLQY of the **PtBDP** films ($\lambda_{exc} = 490$ nm) was around 4%, as a more efficient energy transfer leads to an enhanced Pt-porphyrin emission along with a concomitant increase in the number of photon absorbed from the BDP units.

Table 2. Summary of the electrochemical and EIS features of the reference compounds and **PtBDP** polyads. Electrochemical redox data were recorded in degassed CH_2Cl_2 versus SCE with $TBAPF_6$ as electrolyte. Ferrocene (FcH/FcH^+) ($E^{Ox}_{1/2} = 0.47$ V) was used as the internal standard.

Compound	$Ox1_{BDP}$ [V]	$Ox1_{Por}$ [V]	$Ox2_{Por}$ [V]	$Red1_{BDP}$ [V]	$Red1_{Por}$ [V]	$Red2_{Por}$ [V]	σ [$\times 10^{-8}$ S m^{-1}]
BDP	1.22	–	–	–1.24	–	–	–
Pt-0	–	0.84	1.46	–	–1.64	–	5.93
PtBDP-1-4	1.23	1.07	1.64	–1.22	–1.50	–	3.21
PtBDP-2-8	1.23		–	–1.23		–1.77	3.06
PtBDP-3-12	1.19	1.47	–	–1.22	–1.08	–1.58	0.91
PtBDP-4-16	1.18	1.55	–	–	–0.86	–	0.52
Pt-20	–	1.50	–	–	–0.90	–1.39	0.97

Nevertheless, these PLQY values render them as appealing candidates for NIR LECs compared with those previously reported.[42]

2.3. Electrochemical Characterization in Solution and Thin Films

The electrochemical properties of all reference compounds (**Pt-0**, **Pt-20**, and **BDP**) as well as the final polyads (**PtBDP-1-4**, **PtBDP-2-8**, **PtBDP-3-12**, and **PtBDP-4-16**) were determined by cyclic and square wave voltammetry in freshly distilled and deoxygenated dichloromethane with tetrabutylammonium hexafluorophosphate ($TBAPF_6$) as supporting electrolyte (Figure S57–S62, Supporting Information). All the electrochemical data are shown in **Table 2**.

In line with the literature, **BDP** presents one reversible oxidation and one reversible reduction peak at +1.22 and –1.24 V versus saturated calomel (SCE), respectively. Those peaks are present in the cyclic voltammograms of all final **PtBDP** polyads (**Figure 5**). The *quasi*-reversible redox waves that were shown for the two reference porphyrins (**Pt-0** and **Pt-20**) were located at different regions due to the effect of their different peripheral substituents. Particularly, **Pt-0** presents two oxidation waves at +0.84 and +1.46 V and a reduction wave at –1.64 V (Figure S57, Supporting Information), while **Pt-20** bearing 20 F atoms to the redox peaks were significantly anodically shifted (Figure S58, Supporting Information), namely, one oxidation (+1.50 V) and one reduction wave (–0.90 V). Accordingly, the porphyrin-based redox potentials for the polyads also exhibit anodic shifts in relation to the increasing number of F atoms. This is ascribed to the electron withdrawing properties of the fluorine atoms, resulting in a shift of the oxidation and reduction processes at higher and lower voltages, respectively (Figure 5).

Based on these observations, it is clear that in the final **PtBDP** polyads either one of the constituents gets oxidized or reduced first or both can get oxidized/reduced simultaneously. **PtBDP-1-4** features the first oxidation wave (+1.07 V) related to the Pt-porphyrin core and reduction wave (−1.22 V) of the **BDP** unit, accompanied by other reduction/oxidation features of each moiety—i.e., the oxidation waves of the **BDP** (+1.23 V) and Pt-porphyrin (+1.64 V) and the reduction wave at –1.50 V of the Pt-porphyrin (Figure S59, Supporting Information). As expected, the porphyrin-ascribed peaks are closer to those observed in **Pt-0**,

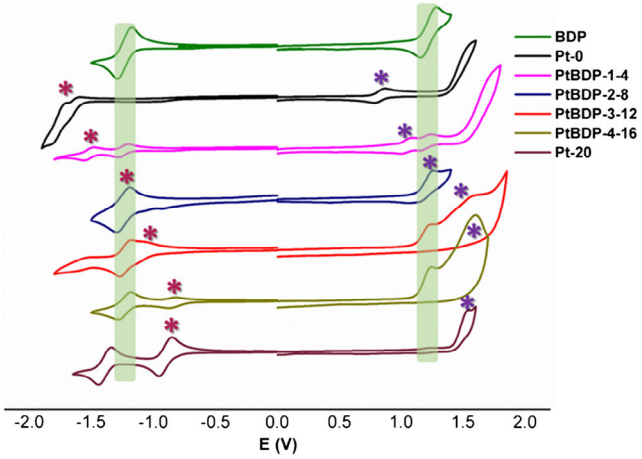

Figure 5. Monitoring the anodically shifted redox potentials in the cyclic voltammograms of our reported systems according to the increasing number of the peripheral fluorine atoms. Green box indicates the stable BDP-centered oxidation and reduction waves, while purple and magenta asterisks highlight the shifts of the first porphyrin-based oxidation and reduction potentials, respectively.

while hole and electron transport processes should be expected via Pt-porphyrin and **BDP** units, respectively. In stark contrast, a single reversible oxidation and reduction wave at +1.23 and −1.23 V were noted for **PtBDP-2-8**, indicating that features from both BDP and the Pt-porphyrin core are very close and, in turn, hole and electron injection might occur in the BDP moiety as expected in a good host:guest system (**Figure 6** and Figure S60, Supporting Information). Conversely, this is not the case for **PtBDP-3-12** that showed the first reversible oxidation and reversible reduction peaks at the **BDP** and the Pt-porphyrin core, respectively (Table 2 and Figure S61, Supporting Information). Thus, hole and electron transport processes will be ruled by the **BDP** and Pt-porphyrin units, respectively. Likewise, **PtBDP-4-16** presents a **BDP**-centered reversible first oxidation at +1.18 V, and a reversible reduction at –0.86 V that is related to the Pt-porphyrin core (Figure S62, Supporting Information) because it is almost the same with the value recorded for **Pt-20** (−0.90 V).

These values were used to calculate the highest occupied molecular orbital (HOMO) and lowest unoccupied molecular orbital (LUMO) levels through the formula $E_{HOMO/LUMO} =$

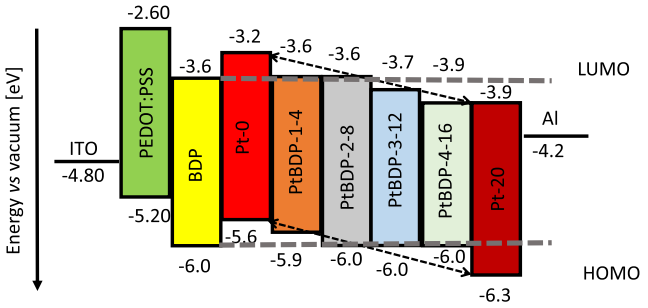

Figure 6. Schematic representation of the HOMO–LUMO energy levels of Pt-0, PtBDP-*x*–*y*, and Pt-20, as calculated from the CV data (with $E_{HOMO/LUMO} = e(V_{Fc}/_{Fc+}) + 4.8$ eV.

$e(V_{Fc}/_{Fc+}) + 4.8$ eV. As such, Figure 6 shows the changes in the electronic structure of the **PtBDP** series in comparison with the energy levels of the device components and reference compounds. With the exception of **PtBDP-1-4**, whose HOMO is located between the **BDP** and **Pt-0** HOMO energy levels, the other polyads' HOMO energy levels are the same to the **BDP** one, indicating that hole injection and transport processes will take place at this moiety. In contrast, the LUMO of **PtBDP-1-4** and **PtBDP-2-8** also corresponds to the **BDP** unit, while for **PtBDP-3-12** and **PtBDP-4-16** their LUMO energy levels are located at the Pt-porphyrin due to influence of the larger number of tetra-fluorophenyl triazole linkers. Thus, only **PtBDP-2-8** shows the best electronic structure to ensure an efficient host: guest scheme that should result in the most stable devices—vide infra.

Finally, electrochemical impedance spectroscopy (EIS) assays were conducted in devices with a standard sandwich architecture (ITO/PEDOT:PSS (70 nm)/active layer (70 nm)/Al) to determine the ionic conductivity (σ) at 0 V—see Experimental Section and Figure S63 and S64, Supporting Information, for the circuit model and Nyquist plots as well as Table S1, Supporting Information. The reference Pt-porphyrin devices showed σ values of 5.3×10^{-8} S m^{-1} (Pt-0) and 9.7×10^{-9} S m^{-1} (Pt-20). This is expected due to the strong interaction between fluorine and the lithium atoms present in the electrolyte.[11] Indeed, there is a clear trend in the **PtBDP** series, in which the σ reduces from 3.2×10^{-8} to 3.1×10^{-8} to 9.1×10^{-9} and to 5.2×10^{-9} S m^{-1} upon increasing the number of F atoms (Table 2). Thus, the increase in the number of the peripheral fluorine atoms may lead to less efficient charge injection and transport affecting the device efficiency—vide infra.

2.4. Device Characterization

As indicated earlier, LECs were prepared with a standard sandwich architecture and measured at a pulsed driving current of 20 mA (**Figure 7**). The figures-of-merit of devices are shown in **Table 3**. Note that the **BDP** device was discarded due to the crystalline morphology of the films. In addition, films consisting of the physical blended **BDP** and Pt-porphyrin reference compounds did not show a homogenous film morphology suitable for device fabrication.

Regardless of the type of emitter, the devices showed the standard LEC behavior as derived from the static EIS assays in the range of 0–4 V. Here, the LEC resistance (R_{LEC}) was plotted against the applied bias, revealing two different slopes, namely, one below the bandgap of the emitters, i.e., 0–2.5 V, and one above it, i.e., 2.5–3 V. The earlier shows a monoexponential slope that resembles the unique feature of LECs with respect to the EDL formation that ultimately lowers the charge injection resistance. In detail, it reduces until 1.5 V and reaches a plateau up to 2.5 V. At applied voltages beyond the bandgap of the emitter, a linear slope is related to an effective ohmic charge injection process that causes the growth of the doped layer. As a result, the electrical resistance in the nondoped region of the film is further reduced, as this region is getting thinner.[43–48]

In line with the static EIS, all the devices showed a similar electroluminescence behavior at pulsed current functioning conditions, that is, a high initial voltage that decreases to a minimum plateau as the p- and n-doped regions are formed and the recombination becomes autosustained in the *i* zone (Figure 7).[4] Finally, the average voltage can arise over time depending on the degradation mechanism and the morphology of the active layer.[45,49] In parallel, the irradiance rises over time until it reaches its maximum value, and it slowly decreases until it reaches half of its maximum. This is defined as lifetime or $t_{1/2}$. Owing to the differences in irradiance values between devices, the device stability is better compared considering the total emitted energy (E_{tot}) of the devices until the irradiance reaches one-fifth of its maximum.[50]

Pt-0- and **Pt-20**-based LECs feature similar irradiances (65 and 48 μW cm^{-2}), luminous efficiencies (0.09 and 0.07 lm W^{-1}), and external quantum efficiencies (EQEs) (0.014% and 0.010%) (Table 3). In both devices, the electroluminescence spectra cover the region from 600 to 900 nm (**Figure 8**). The fresh spectrum shows a well-defined vibrational structure peaking at ≈660 and 790 nm, while the dominant contribution over time is the low-energy emission feature. Compared with the prior examples in porphyrin-based LECs, e.g., 36 μW cm^{-2} at $\lambda_{max} = 900$ nm,[15] these devices already exhibited a remarkable NIR electroluminescence.

All the devices based on the **PtBDP** polyads outperformed the reference devices with both Pt-porphyrins, highlighting the benefits of this molecular design (Table 3 and Figure 7). In detail, the **PtBDP** devices featured a decreasing trend in irradiance and luminous efficiency upon increasing the number of **BDP** units and F atoms (**Figure 9** and Table 3). This is in line with the reduction in ionic conductivity (Table 2) that leads to higher average voltages to hold the applied current. In addition, the stability (E_{tot}) maximizes for the devices based on **PtBDP-2-8** and linearly reduces within the series (Figure 8 and Table 3). Thus, the most balanced devices, showing irradiances of 83 μW cm^{-2}, efficiencies of 0.12 lm W^{-1}, EQEs of 0.030%, and stabilities of 11.1 mJ, are met using the **PtBDP-2-8** compound (Figure 7 and Table 3). This is expected considering the energy levels and the optimized energy transfer processes in thin films (Figure 4 and 6). Within the series, **PtBDP-2-8** exhibits an energy alignment that allows both hole and electron transports to take place at the **BDP** moiety and an efficient energy transfer from the **BDP** to the Pt-porphyrin core, retaining a sufficiently high ionic conductivity—vide supra.

Similar to the reference Pt-porphyrin devices, the electroluminescence spectra show a well-defined emission band located at 660, 720, and 790 nm, with the latter peak's intensity increasing

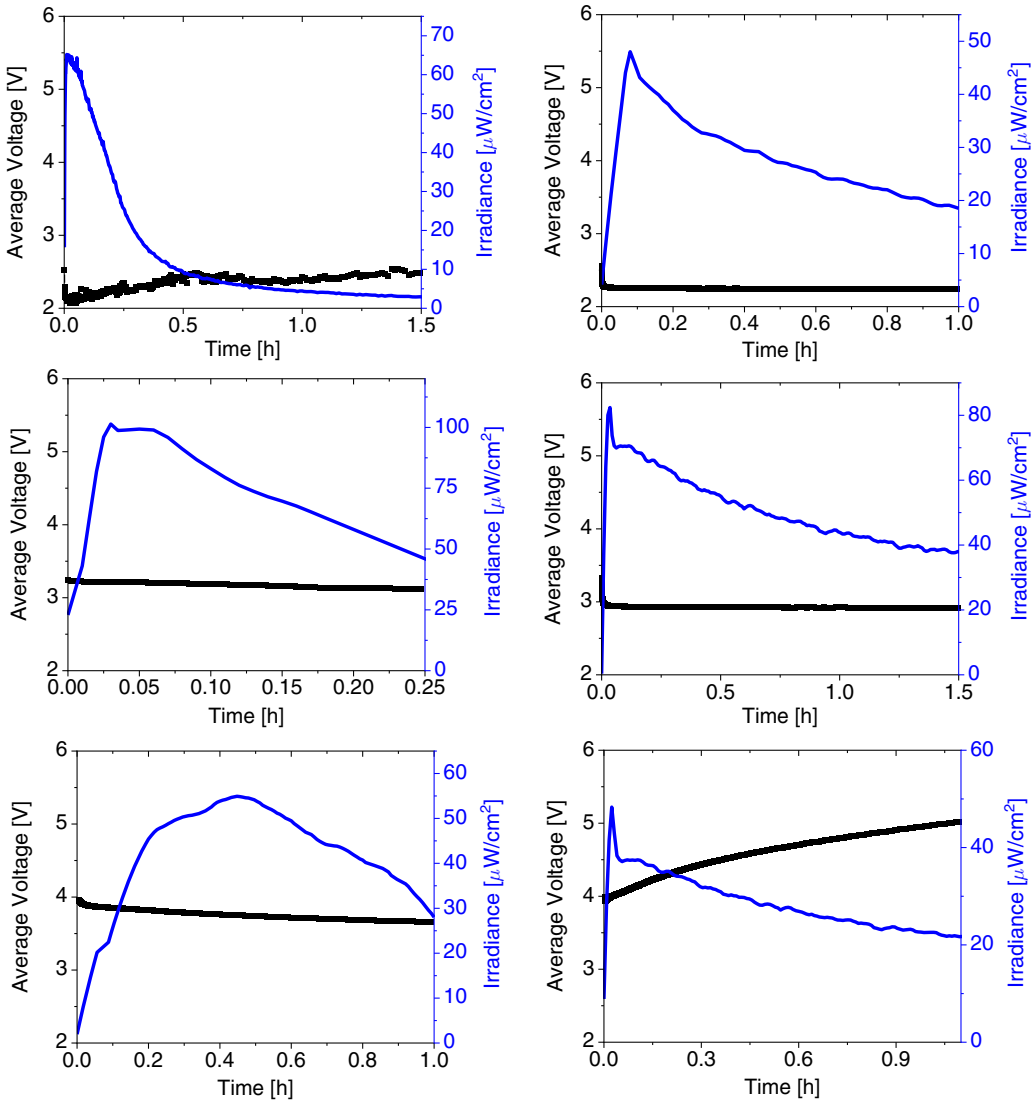

Figure 7. Average voltage and irradiance over time for **Pt-0** (top left), **Pt-20** (top right), **PtBDP-1-4** (center left), **PtBDP-2-8** (center right), **PtBDP-3-12** (bottom left), and **PtBDP-4-16** (bottom right) LECs driven at pulsed 20 mA.

Table 3. Figures-of-merit of devices based on **Pt-0**, **Pt-20**, and **PtBDP** polyads.

Compound	Irradiance$_{max}$ [μW cm^{-2}]	t_{on} [a)] [h]	$t_{1/2}$ [b)] [h]	Efficiency [lmW^{-1}]	EQE [c)] [%]	E_{tot} [d)] [mJ]	λ_{max} [nm]
Pt-0	65.9	0.07	0.20	0.09	0.014	2.37	656, 765
PtBDP-1-4	96.8	0.03	0.25	0.15	0.067	4.04	608, 656, 724, 777
PtBDP-2-8	82.8	0.01	0.81	0.12	0.030	11.1	600, 656, 722, 778
PtBDP-3-12	55.7	0.52	1.1	0.06	0.022	10.7	610, 656, 778
PtBDP-4-16	49.1	0.03	1.0	0.06	0.012	8.81	528, 600, 656, 791
Pt-20	48.2	0.10	0.92	0.06	0.010	7.39	542, 610, 656, 778

[a)]Turn on time: time to reach the maximum luminance; [b)]Lifetime: time to reach 50% of the maximum luminance; [c)]EQE: it describes the ratio of emitted photons per injected electrons; [d)]Total emitted energy: calculated from integration of the radiant flux of the device versus time from $t = 0$ to $t = t_{1/5}$.

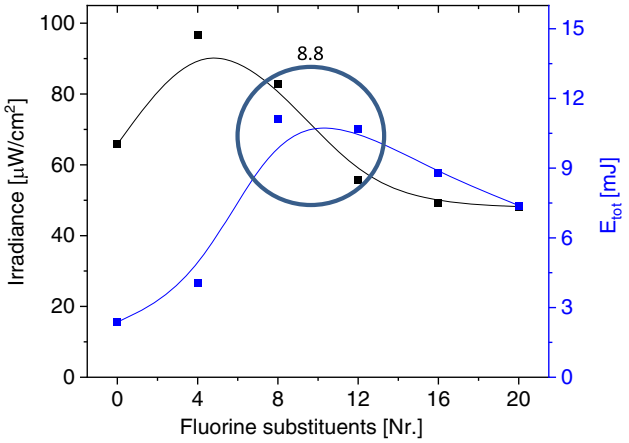

Figure 8. Irradiance and total emitted energy versus the number of F atoms in **Pt-0** and **Pt-20** and **PtBDP** polyads. The circle highlights the area including the devices, in which both parameters are maximized. The intersection between the two curves corresponds to a number of fluorine substituents of 8.8, as highlighted in the graph.

over time (Figure 9). Electroluminescence features of the **BDP** unit were not observed, indicating that the energy transfer between the **BDP** moiety and the Pt-por is quantitative under device operation conditions. Note that the electroluminescence spectrum shows different relative intensity of each resonant peak with the photoluminescence spectrum (Figure 4 and 9). This could be related to interference effect from the device optical structure, self-absorption of doped species, and the changes in the radiative rates of the vibrational states of the excited state caused by the effects of external and local electrical fields.

Overall, the high irradiance values (e.g., 83 $\mu W\,cm^{-2}$ for **PtBDP-2-8**) are considerably high for a pure NIR emission, while the limited stability of the material could be overcome by optimizing driving scheme using, for example, intermittent operation as shown by Gao's group.[51]

3. Conclusions

We report on the synthesis, characterization, and LEC device application of a series of NIR-emitting Pt-porphyrin-based systems including two reference Pt-por and four **PtBDP** polyads, in which the number of **BDP** groups and fluorine atoms gradually increases. This ruled the energy transfer process from **BDP** to Pt-porphyrin core, the electronic structure toward an effective host:guest scheme, and the ionic conductivity in thin films. This was established via a one-to-one comparison of the spectroscopic and electrochemical features in accordance to the device behavior within this series. In general, the **PtDBP** polyad design led to devices outperforming the Pt-porphyrin references. In particular, the **PtBDP** containing two **BDP** units and eight F atoms led to superior devices with irradiances of 83 $\mu W\,cm^{-2}$, efficiencies of 0.12 $lm\,W^{-1}$, E_{tot} of 11 mJ, and at a low-energy electroluminescence maximum centered at $\lambda_{max} \approx 780$ nm. This result is attributed to a trade-off between the electronic alignment toward an effective intramolecular host–guest system, an efficient energy transfer, and a reduction of the ionic conductivity to achieve high irradiances and stabilities. Overall, this work gives important molecular design guidelines on the preparation of efficient low-energy emitting sustainable porphyrin-based emitters for application in NIR lighting technologies.

4. Experimental Section

Materials and Techniques: All chemicals and solvent were purchased in reagent grade from commercial suppliers and directly used, unless otherwise stated. NMR spectra were recorded on a Bruker AVANCE III-500 MHz spectrometer, selecting the deuterated solvent peak as the internal standard. Mass spectra were obtained with an UltrafleXtreme matrix-assisted laser desorption ionization time-of-flight (MALDI-TOF) spectrometer (Bruker), selecting *trans*-2-[3-(4-tert-butylphenyl)-2-methyl-2-propenylidene] malononitrile (DCTB) as matrix. In the Supporting Information, we provide further information regarding the synthesis of all intermediate and final derivatives.

Fabrication and Characterization of Solutions and Thin Films: A Shimatzu 2700-I UV–Vis spectrometer was used to acquire UV–vis spectral data. Photoluminescence spectra and PLQY values were obtained with a FS5 spectrofluorometer with integrating sphere (Edinburgh Instruments), while average excited states lifetimes (t) were measured with an Edinburgh Instruments TCSPC and exciting either with a diode laser ($\lambda_{exc} = 377$ nm) or a microsecond lamp (100 Hz frequency).

The average lifetime was calculated with the following formula:[52] $R(t) = \sum_{i=1}^{2} A_i e^{\frac{-t}{\tau_i}}$, where A_i is constant. In our case (double-component decay), the average lifetime equals to:

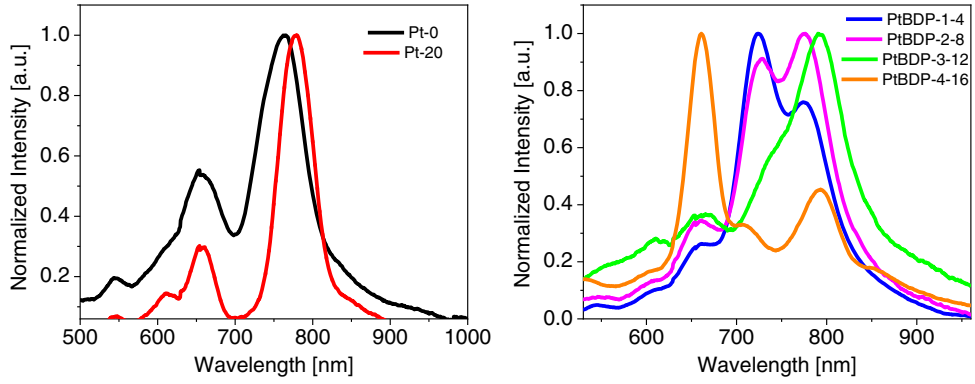

Figure 9. Electroluminescence spectra of **Pt-0** and **Pt-20** (left, see legend), and **PtBDP** polyads (right, see legend).

$$\langle\tau\rangle = \frac{A_1\tau_1^2 + A_2\tau_2^2}{A_1\tau_1 + A_2\tau_2} \quad (1)$$

To achieve thin films on a quartz substrate, a THF solution of the emitter with a concentration of 12 mg mL^{-1} was used to spin-coat thin films under nitrogen pressure with the following three-step procedure: 700 rpm for 30 s, 1600 rpm for 30 s, and 3000 rpm for 10 s. The resulting thickness was 70 nm. The used spin-coater is a Laurell WS-650mz-23npbb. The morphology of the thin films was checked via AFM assays with a Park XE150 instrument (Park Systems Corp., Suwon, South Korea).

Electrochemical Characterization in Solution: Cyclic and square wave voltammetry assays were performed with an AutoLab PGSTAT20 potentiostat, using a scan rate of 100 mV s^{-1}, in deoxygenated CH_2Cl_2 solutions featuring tetrabutylammonium hexafluorophosphate 0.1 M ($TBAPF_6$) as supporting electrolyte. The cell setup consisted in a glassy carbon working electrode, a SCE reference electrode, and a platinum wire as counter electrode. The ferrocene/ferrocenium couple was employed in all cases as reference (0.46 V vs SCE).

Device Preparation and Characterization: ITO substrates (130 nm thick) (Naranjo Substrates) were carefully cleaned by bathing them in soap, water, ethanol, and isopropanol in an ultrasonic bath for 15 min each. Then, they were put in a UV–ozone cleaner for 8 min. Right after this step, a PEDOT:PSS layer (70 nm) was spin-coated on top of the clean substrates. In detail, the PEDOT:PSS (Clevios Ai 4083) was mixed with isopropanol in a volumetric ratio of 3:1.3, and spin-coated onto the plates at 1700 rpm for 60 s. An annealing step followed (30 min, 120 °C). The BDP-Pt-por polyad were spin-coated on top of the PEDOT:PSS from a 10 mg mL^{-1} THF solution containing the electrolyte matrix in a weight ratio of polyad:TMPE (M_w 450 000):LiOTf 1:0.15:0.03. This spin coating procedure consisted in three steps: 700 rpm for 30 s, 1600 rpm for 30 s, and 3000 rpm for 10 s. The thickness of the layers was of 70 nm, as measured from an AlphaStep 500 profilometer (KLA Tencor). The devices were dried under vacuum for 2 h before being inserted in a glove box (<0.1 ppm O_2 and H_2O, Angstrom Engineering), where 90 nm-thick aluminum cathodes were evaporated under physical vapor deposition a in high vacuum Angstrom Covap evaporator. The device active area was of 10 mm^2. The so-fabricated LECs were measured with the coupled Avantes spectrophotometers Avaspec-ULS2048L-USB2 and AvaSpec-ULS2048CL-EVO for high UV–Vis and NIR sensitivity, respectively, and a calibrated integrated sphere Avasphere 30-Irrad and a Botest OLT OLED Lifetime-Test System, as described in previous contributions.[13,53] EIS assays were conducted with a potentiostat/galvanostat PGSTAT204 (Metrohm μAutolabIII) with EIS frequency response analyser module (FRA2). The applied voltage ranged from 0 to 4 V. The obtained data were fitted with the Nova software 1.1 using the circuit model shown in Figure S63, Supporting Information, as described in previous contributions.[13]

Supporting Information

Supporting Information is available from the Wiley Online Library or from the author.

Acknowledgements

E. F. and A.C. contributed equally to this work. E.F. and R.D.C. acknowledge the HYNANOSC (RTI2018-099504-A-C22) and the FOTOART-CM project funded by Madrid region under program P2018/NMT-4367. This research was funded by the General Secretariat for Research and Technology (GSRT) and Hellenic Foundation for Research and Innovation (HFRI; project code: 508). This research has also been cofinanced by the European Union and Greek national funds through the Operational Program Competitiveness, Entrepreneurship, and Innovation, under the call RESEARCH–CREATE–INNOVATE (project code: T1EDK-01504). Furthermore, this research has been cofinanced by the European Union and Greek national funds through the Regional Operational Program "Crete 2014-2020," project code OPS:5029187. Moreover, the European Commission's Seventh Framework Program (FP7/2007-2013) under grant agreement no. 229927 (FP7-REGPOT-2008-1, Project BIO-SOLENUTI) and the Special Research Account of the University of Crete are also acknowledged for the financial support of this research.

Conflict of Interest

The authors declare no conflict of interest.

Data Availability Statement

Research data are not shared.

Keywords

carrier trapping, host:guest, light-emitting electrochemical cells, near-infrared emission, porphyrin polyads

Received: December 15, 2020
Revised: March 12, 2021
Published online: May 21, 2021

[1] S. Kanagaraj, A. Puthanveedu, Y. Choe, *Adv. Funct. Mater.* **2020**, *30*, 1907126.
[2] K. Matsuki, J. Pu, T. Takenobu, *Adv. Funct. Mater.* **2020**, *30*, 1908641.
[3] E. Fresta, R. D. Costa, *J. Mater. Chem. C* **2017**, *5*, 5643.
[4] R. D. Costa, *Light-Emitting Electrochemical Cells. Concepts, Advances and Challenges*, Springer International Publishing, Basel **2017**.
[5] J. Xu, A. Sandström, E. M. Lindh, W. Yang, S. Tang, L. Edman, *ACS Appl. Mater. Interfaces* **2018**, *10*, 33380.
[6] S. Tang, L. Edman, *Top. Curr. Chem.* **2016**, *374*, 40.
[7] E. Auroux, A. Sandström, C. Larsen, P. Lundberg, T. Wågberg, L. Edman, *Org. Electron.* **2020**, *84*, 105812.
[8] G. Hernandez-Sosa, A. J. Morfa, N. Jürgensen, S. Tekoglu, J. Zimmermann, in *Light-Emitting Electrochemical Cells: Concepts, Advances and Challenges*, Springer International Publishing, Basel **2017**, pp. 139–163.
[9] A. F. Henwood, E. Zysman-Colman, *Top. Curr. Chem.* **2016**, *374*, 36.
[10] E. Fresta, M. D. Weber, J. Fernández-Cestau, R. D. Costa, *Adv. Opt. Mater.* **2019**, *7*, 1900830.
[11] M. D. Weber, V. Nikolaou, J. E. Wittmann, A. Nikolaou, P. A. Angaridis, G. Charalambidis, C. Stangel, A. Kahnt, A. G. Coutsolelos, R. D. Costa, *Chem. Commun.* **2016**, *52*, 1602.
[12] H. J. Bolink, L. Cappelli, E. Coronado, P. Gaviña, *Inorg. Chem.* **2005**, *44*, 5966.
[13] E. Fresta, K. Baumgärtner, J. Cabanillas-Gonzalez, M. Mastalerz, R. D. Costa, *Nanoscale Horiz.* **2020**, *5*, 473.
[14] S. Tang, W.-Y. Tan, X.-H. Zhu, L. Edman, *Chem. Commun.* **2013**, *49*, 4926.
[15] M. Mone, S. Tang, P. Murto, B. A. Abdulahi, C. Larsen, J. Wang, W. Mammo, L. Edman, E. Wang, *Chem. Mater.* **2019**, *31*, 9721.
[16] M. D. Weber, M. Adam, R. R. Tykwinski, R. D. Costa, *Adv. Funct. Mater.* **2015**, *25*, 5066.
[17] K. T. Weber, K. Karikis, M. D. Weber, P. B. Coto, A. Charisiadis, D. Charitaki, G. Charalambidis, P. Angaridis, A. G. Coutsolelos, R. D. Costa, *Dalt. Trans.* **2016**, *45*, 13284.

[18] Z. B. Hill, D. B. Rodovsky, J. M. Leger, G. P. Bartholomew, *Chem. Commun.* **2008**, 6594.
[19] S. Jenatsch, L. Wang, M. Bulloni, A. C. Véron, B. Ruhstaller, S. Altazin, F. Nüesch, R. Hany, *ACS Appl. Mater. Interfaces* **2016**, *8*, 6554.
[20] A. Pertegás, D. Tordera, J. Serrano-Pérez, *J. Am. Chem. Soc.* **2013**, *135*, 18008.
[21] B. Pashaei, S. Karimi, H. Shahroosvand, M. Pilkington, *Adv. Funct. Mater.* **2020**, *30*, 1908103.
[22] B. Pashaei, S. Karimi, H. Shahroosvand, P. Abbasi, M. Pilkington, A. Bartolotta, E. Fresta, J. Fernandez-Cestau, R. D. Costa, F. Bonaccorso, *Chem. Soc. Rev.* **2019**, *48*, 5033.
[23] R. D. Costa, E. Ortí, H. J. Bolink, F. Monti, G. Accorsi, N. Armaroli, *Angew. Chem. Int. Ed.* **2012**, *51*, 8178.
[24] W. Xiong, S. Tang, P. Murto, W. Zhu, L. Edman, E. Wang, *Adv. Opt. Mater.* **2019**, *7*, 1900280.
[25] B. N. Bideh, C. Roldán-Carmona, H. Shahroosvand, M. K. Nazeeruddin, *J. Mater. Chem. C* **2016**, *4*, 9674.
[26] B. Nemati Bideh, H. Shahroosvand, *New J. Chem.* **2020**, *44*, 1881.
[27] B. Nemati Bideh, H. Shahroosvand, *Sci. Rep.* **2017**, *7*, 15739.
[28] A. Barbieri, E. Bandini, F. Monti, V. K. Praveen, N. Armaroli, *Top. Curr. Chem.* **2016**, *374*, 47.
[29] S. Tang, P. Murto, J. Wang, C. Larsen, M. R. Andersson, E. Wang, L. Edman, *Adv. Opt. Mater.* **2019**, *7*, 1900451.
[30] T. Lazarides, G. Charalambidis, A. Vuillamy, M. Réglier, E. Klontzas, G. Froudakis, S. Kuhri, D. M. Guldi, A. G. Coutsolelos, *Inorg. Chem.* **2011**, *50*, 8926.
[31] T. Lazarides, S. Kuhri, G. Charalambidis, M. K. Panda, D. M. Guldi, A. G. Coutsolelos, *Inorg. Chem.* **2012**, *51*, 4193.
[32] K. Ladomenou, V. Nikolaou, G. Charalambidis, A. Charisiadis, A. G. Coutsolelos, *Comptes Rendus Chim.* **2017**, *20*, 314.
[33] V. Nikolaou, A. Charisiadis, S. Chalkiadaki, I. Alexandropoulos, S. C. Pradhan, S. Soman, M. K. Panda, A. G. Coutsolelos, *Polyhedron* **2018**, *140*, 9.
[34] J. K. Laha, S. Dhanalekshmi, M. Taniguchi, A. Ambroise, J. S. Lindsey, *Org. Process Res. Dev.* **2003**, *7*, 799.
[35] K. E. Splan, J. T. Hupp, *Langmuir* **2004**, *20*, 10560.
[36] H. C. Sample, M. O. Senge, *Eur. J. Org. Chem.* **2020**, *2021*, 7.
[37] J. Y. Liu, M. E. El-Khouly, S. Fukuzumi, D. K. P. Ng, *Chem. – A Eur. J.* **2011**, *17*, 1605.
[38] D. Samaroo, M. Vinodu, X. Chen, C. M. Drain, *J. Comb. Chem.* **2007**, *9*, 998.
[39] T. V. Goud, A. Tutar, J. F. Biellmann, *Tetrahedron* **2006**, *62*, 5084.
[40] E. Fresta, M. Monclus, M. Bertz, C. Ezquerro, J. Molina, J. R. Berenguer, M. Kunimoto, T. Homma, R. D. Costa, *Adv. Opt. Mater.* **2020**, *8*, 2000295.
[41] O. Exner, S. Böhm, *New J. Chem.* **2008**, *32*, 1449.
[42] R. Englman, J. Jortner, *Mol. Phys.* **1970**, *18*, 285.
[43] S. Van Reenen, R. A. J. Janssen, M. Kemerink, *Adv. Funct. Mater.* **2012**, *22*, 4547.
[44] S. van Reenen, P. Matyba, A. Dzwilewski, R. A. J. Janssen, L. Edman, M. Kemerink, *J. Am. Chem. Soc.* **2010**, *132*, 13776.
[45] S. B. Meier, D. Hartmann, A. Winnacker, W. Sarfert, *J. Appl. Phys.* **2014**, *116*, 104504.
[46] A. Munar, A. Sandström, S. Tang, L. Edman, *Adv. Funct. Mater.* **2012**, *22*, 1511.
[47] B. M. D. Puscher, M. F. Aygüler, P. Docampo, R. D. Costa, *Adv. Energy Mater.* **2017**, *7*, 1602283.
[48] E. Fresta, J. Dosso, J. Cabanillas-Gonzalez, D. Bonifazi, R. D. Costa, *Adv. Funct. Mater.* **2020**, *30*, 1906830.
[49] E. Fresta, G. Volpi, M. Milanesio, C. Garino, C. Barolo, R. D. Costa, *Inorg. Chem.* **2018**, *57*, 10469.
[50] G. Kalyuzhny, M. Buda, J. Mcneill, P. Barbara, A. J. Bard, *J. Am. Chem. Soc.* **2003**, *125*, 6272.
[51] F. Altal, J. Gao, *Org. Electron.* **2015**, *18*, 1.
[52] C. M. Luk, L. B. Tang, W. F. Zhang, S. F. Yu, K. S. Teng, S. P. Lau, *J. Mater. Chem.* **2012**, *22*, 22378.
[53] E. Fresta, J. Dosso, J. Cabanillas-Gonzalez, D. Bonifazi, R. D. Costa, *ACS Appl. Mater. Interfaces* **2020**, *12*, 28426.